Detection of Spectral Signatures in Multispectral MR Images for Classification

Chuin-Mu Wang, Clayton Chi-Chang Chen, Yi-Nung Chung, Sheng-Chih Yang, Pau-Choo Chung, Ching-Wen Yang, and Chein-I. Chang*, *Senior Member, IEEE*

Abstract—**This paper presents a new spectral signature detection approach to magnetic resonance (MR) image classification. It is called constrained energy minimization (CEM) method, which is derived from the minimum variance distortionless response in passive sensor array processing. It considers a bank of spectral channels as an array of sensors where each spectral channel represents a sensor and object spectral signature in multispectral MR images are viewed as signals impinging upon the array. The strength of the CEM lies on its ability in detection of spectral signatures of interest without knowing image background. The detected spectral signatures are then used for classification. The CEM makes use of a finite impulse response (FIR) filter to linearly constrain a desired object while minimizing interfering effects caused by other unknown signal sources. Unlike most spatial-based classification techniques, the proposed CEM takes advantage of spectral characteristics to achieve object detection and classification. A series of experiments is conducted and compared with the commonly used *c*-means method for performance evaluation. The results show that the CEM method is a promising and effective spectral technique for MR image classification.**

I. INTRODUCTION

NUCLEAR magnetic resonance (NMR) can be used to measure the nuclear spin density, the interactions of the nuclei with their surrounding molecular environment and those between close nuclei, respectively. It produces a sequence of multiple spectral images of tissues with a variety of contrasts using three magnetic resonance parameters, spin-lattice (T1), spin–spin (T2), and dual echo–echo proton density (PD). By appropriately choosing pulse sequence parameters, echo time (TE), and repetition time (TR), a sequence of images of specific anatomic area can be generated by pixel intensities that represent characteristics of different types of tissues throughout the sequence. Additionally, the spectral correlation among the image sequence produces information that spatial correlation cannot provide. As a result, magnetic resonance imaging (MRI) becomes a more useful image modality than X-ray computerized tomography (X-CT) when it comes to analysis of soft tissues and organs since the information about T1 and T2 offers a more precise picture of tissue functionality than that produced by X-CT [1], [2]. Over the past years many computer-assisted methods have been reported in the literature [3]–[20] such as PCA in [6], eigenimage analysis in [7]–[12], neural networks [13]–[16], fuzzy *c*-means (CM) methods [17], [18], hybrid methods [19], knowledge-based techniques [20], orthogonal projection [21], etc. For example, eigenimage filtering-based approach has shown a promise in segmentation and feature extraction. Hybrid methods combine imaging processing and model-based techniques to improve segmentation. Knowledge-based techniques further allow one to make more intelligent classification and segmentation decisions. As an alternative, neural networks are also proposed to demonstrate their superior performance in segmentation of brain tissues to classical maximum-likelihood methods. More recently, an orthogonal subspace projection approach to MR image classification was proposed in [21], which used an orthogonal subspace projector in conjunction with a matched filter to extract desired objects while annihilating undesired objects.

In this paper, we make a distinction between pattern classification and object classification. In pattern classification, a classifier must classify image data into a number of pattern classes, which also include background classes. Although the background knowledge may be obtained directly from the image data in an unsupervised means, it may not be accurate. In some cases, it may not be reliable, particularly, when the objects are relatively small or the image background are complicated. Besides, image background generally varies with pixels and is difficult to characterize. As a result, it is nearly impossible to classify image background without complete background knowledge. On the other hand, in object classification we are generally interested in classification of objects of interest, but not classification of image background. In many situations, we may have prior knowledge about the objects we would like to classify, but do not have knowledge about image background. Under such circumstance, it is highly desirable to perform object classification with no need of acquiring

background knowledge. This paper presents a new approach to object classification for MR images, called constrained energy minimization (CEM) developed in [22]–[25], which resolves this dilemma.

The CEM has shown great success in hyperspectral target detection and classification. It was designed based on a premise that no background information is required for target detection. More specifically, the only working knowledge for the CEM is the desired target. This advantage is particularly significant when the desired targets are present in an image with complicated background that involves many unknown and unidentified targets which are not of our interest. In MRI classification, it often occurs that the objects in which we are interested are known *a priori* while complete knowledge of the image background may not be available due to its complexity resulting from variabilities of tissues' characterization. Therefore, if we interpret desired targets as objects of interest the CEM fits well in object classification in MR images. In analogy with the way that the CEM is applied to a hyperspectral image, the CEM treats an MR image as an image cube with each image pixel considered to be a column vector. So, it takes advantage of spectral information provided by different bands in a single pixel vector as well as spectral correlation among sample pixel vectors. This benefit cannot be obtained by spatial analysis-based techniques. In medical imaging, the objects of interest are generally soft tissues that are deformable and cannot be analyzed by their shapes. The CEM is a spectral-based technique that does not rely its classification on object shapes. Consequently, the CEM may be more effective in soft object classification than classical spatial analysis-based image processing classification techniques that utilize sample spatial information and correlation.

The proposed CEM method is derived from the minimum variance distortionless response (MVDR) approach that arises in sensor array processing [26]–[28]. It casts an MR image classification problem as a direction finding for signal arrival from an adaptive beamforming array. It interprets a bank of spectral bands as an array of passive sensors where each spectral band is considered as a sensor and an object present in an MR image sequence is viewed as a signal impinging upon the array. More specifically, if we consider an MR image pixel as a vector, two features that completely determine the vector are its direction and its vector length. So, if two pixel vectors pointing to the same direction, they will be considered to be in the same class with different magnitudes determined by their vector lengths. In the MVDR, signal arrival from a desired direction is generally assumed to be known *a priori*. Then it designs an adaptive filter to pass through the desired signal using a unity filter constraint (i.e., scalar 1) while the filter output variance (i.e., energy) is minimized. In MRI classification, the CEM filter interprets the desired direction of signal arrival as the direction pointed by a particular object pixel vector. So, all the pixel vectors pointing to the same direction will belong to the same pattern class and will be passed by the CEM filter with a unity constraint while the energies (i.e., vector lengths) of pixel vectors pointing to other directions will be minimized. With this interpretation the CEM filter classifies an object in an unknown image background in an MR image sequence by constraining its vector direction while minimizing the effects resulting from other directions. In this

case, the pixel vectors which produce directions other than the desired direction will be considered as interfering pixel vectors and their energies will be minimized in the output of the CEM filter. There is no need of knowing these interfering pixel vectors that may include unknown background pixels and unidentified signal source vectors. This suggests that finding a CEM filter is equivalent to seeking an adaptive beamformer, which locks on the desired direction of signal arrival with a unity constraint. The weights chosen for the CEM filter to extract the desired object vectors while minimizing the energies of other pixel vectors are the same as those chosen for an adaptive beamformer that passes signals coming from desired directions while minimizing the output variance caused by signals coming from other directions. Accordingly, it is not surprising to see that the same success found in the MVDR approach is also applied to MR image classification.

The experimental results demonstrate that the CEM filter has shown its ability in detection and classification of object spectral signatures in an MR image sequence. In order to further evaluate its performance, the CM method [29] is used for comparison. Unlike the CEM that performs object classification, the CM method is a pattern classification technique, which must assign each image pixel to one of pattern classes. The CM method implemented in this paper is slightly different from the one commonly used in the literature. Since the CEM filter requires the knowledge of objects of interest, in order for a fair comparison, the used CM method also includes this prior knowledge in its clustering procedure. Nevertheless, the CM method is still considered to be unsupervised because it needs to generate class information in an unsupervised manner, which is not provided *a priori*. As will be shown, the CM method does not perform as well as does the CEM filter due to the fact that it is a spatial analysis-based pattern classification technique.

The remainder of this paper is organized as follows. Section II presents the CEM approach. Section III briefly describes a modified version of the CM method to be implemented in this paper. Section IV conducts a series of experiments to evaluate the effectiveness of CEM in classification performance and also compare the results to those produced by the CM method. Section V concludes some comments.

II. Constrained Energy Minimization Approach

Let L be the number of spectral bands (channels) used to acquire MR image sequences. In this case, an MR image sequence is actually a collection of co-registered L spectral bands. So, an ith image pixel in an MR image sequence can be considered as an L-dimensional pixel vector, denoted by $\mathbf{r}_i = (r_{i1}, r_{i2}, \ldots, r_{iL})^T$ where r_{ij} represents the pixel of the ith pixel vector in the jth spectral band. Suppose that $\{\mathbf{r}_1, \mathbf{r}_2, \ldots, \mathbf{r}_N\}$ is a set of all image pixels in an MR image sequence where N is the total number of pixels in the image. Let $\mathbf{d}$ be the spectral signature of an object of interest. The goal is to design a finite impulse response (FIR) linear filter specified by an L-dimensional vector $\mathbf{w} = (w_1, w_2, \ldots, w_L)^T$ that passes the desired signature $\mathbf{d}$ by constraining its direction while minimizing its output energy that are caused by signal source vectors with directions other than the constrained direction.

More specifically, let y_i denote the output of the designed FIR filter resulting from the ith MR image pixel $\mathbf{r}_i$. Then y_i can be expressed by

$$y_i = \sum_{l=1}^{L} w_l r_{il} = \mathbf{w}^T \mathbf{r}_i = \mathbf{r}_i^T \mathbf{w}. \tag{1}$$

The average filter output energy resulting from $\{\mathbf{r}_1, \mathbf{r}_2, \ldots, \mathbf{r}_N\}$ is given by

$$\frac{1}{N} \left[\sum_{i=1}^{N} y_i^2 \right] = \frac{1}{N} \left[\sum_{i=1}^{N} (\mathbf{r}_i^T \mathbf{w})^T \mathbf{r}_i^T \mathbf{w} \right]$$

$$= \mathbf{w}^T \left(\frac{1}{N} \left[\sum_{i=1}^{N} \mathbf{r}_i \mathbf{r}_i^T \right] \right) \mathbf{w} = \mathbf{w}^T \mathbf{R}_{L \times L} \mathbf{w} \tag{2}$$

where $\mathbf{R}_{L \times L} = (1/N)[\sum_{i=1}^{N} \mathbf{r}_i \mathbf{r}_i^T]$ is the auto-correlation sample matrix of the MR image sequence. So, the CEM filter is one solving the following linearly constrained optimization problem

$$\min_{\mathbf{w}} \{ \mathbf{w}^T \mathbf{R}_{L \times L} \mathbf{w} \} \text{ subject to } \mathbf{d}^T \mathbf{w} = 1. \tag{3}$$

The solution to (3) is given in [22]–[25] by

$$\mathbf{w}^* = \frac{\mathbf{R}_{L \times L}^{-1} \mathbf{d}}{\mathbf{d}^T \mathbf{R}_{L \times L}^{-1} \mathbf{d}}. \tag{4}$$

Substituting the optimal weight given by (4) for $\mathbf{w}$ in (1) yields the CEM filter which implements a detector, $\delta_{\text{CEM}}(\mathbf{r})$ on an image pixel vector $\mathbf{r}$ and is given by

$$\delta_{\text{CEM}}(\mathbf{r}) = (\mathbf{w}^*)^T \mathbf{r} = \left(\frac{\mathbf{R}_{L \times L}^{-1} \mathbf{d}}{\mathbf{d}^T \mathbf{R}_{L \times L}^{-1} \mathbf{d}} \right)^T \mathbf{r} = \frac{\mathbf{d}^T \mathbf{R}_{L \times L}^{-1} \mathbf{r}}{\mathbf{d}^T \mathbf{R}_{L \times L}^{-1} \mathbf{d}}. \tag{5}$$

As we can see from (5), when $\mathbf{r} = \mathbf{d}$, $\delta_{\text{CEM}}(\mathbf{d}) = 1$ which satisfies the constraint in (3). In this case, the $\mathbf{r}$ is considered to be the desired object pixel and will be extracted by the CEM filter. Despite that the primary task of the CEM filter is object detection, as demonstrated in the experiments it can perform as a classifier by detecting different types of objects, one at a time. In this case, separate images are produced for each type of targets.

A comment is noteworthy. The value of $\delta_{\text{CEM}}(\mathbf{r})$ resulting from (5) represents the estimated abundance fraction of the object signature $\mathbf{d}$ contained in the image pixel $\mathbf{r}$. So, unlike most spatial-based classification methods that can be considered as label (class)-assignment techniques, the CEM filter detects a desired object by estimating its abundance fraction using (5). As a result, the image generated by the CEM filter is generally gray scale where the gray level value of each image pixel reflects the detected amount of the abundance fraction of the desired object present in the pixel. The object detection is then performed based on the resulting gray scale image and classification is carried out by detecting the desired objects in separate images.

III. C-MEANS (CM) METHOD

In order to evaluate performance of the CEM approach, the widely used CM method [29] (also known as k-means in [30])

is used for comparative analysis. The reason to select the CM method is twofold. One is that it allows us to generate background signatures in an unsupervised manner for classification. Another is that it is basically a spatial-based pattern classification technique. As opposed to the CEM approach that only classifies objects of interest, the CM method classifies all MR image pixel vectors including background pixel vectors into pattern classes.

The CM method to be implemented in this paper for experiments is a modified version of the commonly used CM method, which is also referred to as ISODATA in [29], [30]. In order to make a fair comparison, the CM method used here includes into its clustering procedure the same knowledge of objects of interest that is required by the CEM approach. Let the spectral signatures of p objects of interest be denoted by $\{\mathbf{d}_i\}_{i=1}^{p}$ where $\mathbf{d}_i$ is the spectral signature of the ith object. The detailed implementation of the CM method can be described as follows.

CM Method

1) Determine the number of pattern classes, $c \geq p$ and let $\{\mu_i\}_{i=1}^{c}$ be their corresponding class means.
2) Initialization:
   Let $k = 0$ and the first p class means is fixed at $\mu_i^{(0)} = \mathbf{d}_i$, $1 \leq i \leq p$ where $\{\mathbf{d}_i\}_{i=1}^{p}$ are provided by prior knowledge as required by the CEM filter. All other class means $\mu_i^{(0)}$, $i > p$ are selected randomly. That is, for $p+1 \leq i \leq c$, choose any initial value other than $\{\mathbf{d}_i\}_{i=1}^{p}$ for the ith class mean $\mu_i^{(0)}$.
3) At the kth iteration, compute the distance of each sample pixel vector from all class means, $\mu_i^{(k)}$ for $1 \leq i \leq c$ and assign the sample vector to the class whose mean has the shortest distance to the sample vector.
4) For each class i with $p + 1 \leq i \leq c$, recompute its class mean by averaging the sample vectors in the class, denoted by $\hat{\mu}_i^{(k)}$.
   Let $k \leftarrow k+1$, $\mu_i^{(k)} = \mathbf{d}_i$, $1 \leq i \leq p$ and $\mu_i^{(k)} \leftarrow \hat{\mu}_i^{(k)}$ for $p + 1 \leq i \leq c$.
5) If any class mean changes in the set $\{\mu_i^{(k)}\}_{i=p+1}^{c}$, go to step 3).

It should be noted that the knowledge of $\{\mathbf{d}_i\}_{i=1}^{p}$ is given *a priori*. Therefore, the first p class means are fixed during iterations. However, the class means, $\{\mu_i^{(k)}\}_{i=p+1}^{c}$ are regenerated at each iteration by the CM method in an unsupervised manner using the minimum distance as a criterion. These generated class means are considered to be signatures of unknown signal sources, which are not provided by prior knowledge and may include background signatures. Since the CM method is a pattern classification technique, one of its weaknesses is determination of c, i.e., the number of pattern classes. If c is too small, the number of c pattern classes may not well represent the data, in which several distinct classes may be merged into one class. If c is too large, the number of c pattern classes may over-represent the data, in which a class may be forced to be broken up into several classes. The CEM resolves this dilemma by performing object classification without using any information other than that provided by $\{\mathbf{d}_i\}_{i=1}^{p}$.
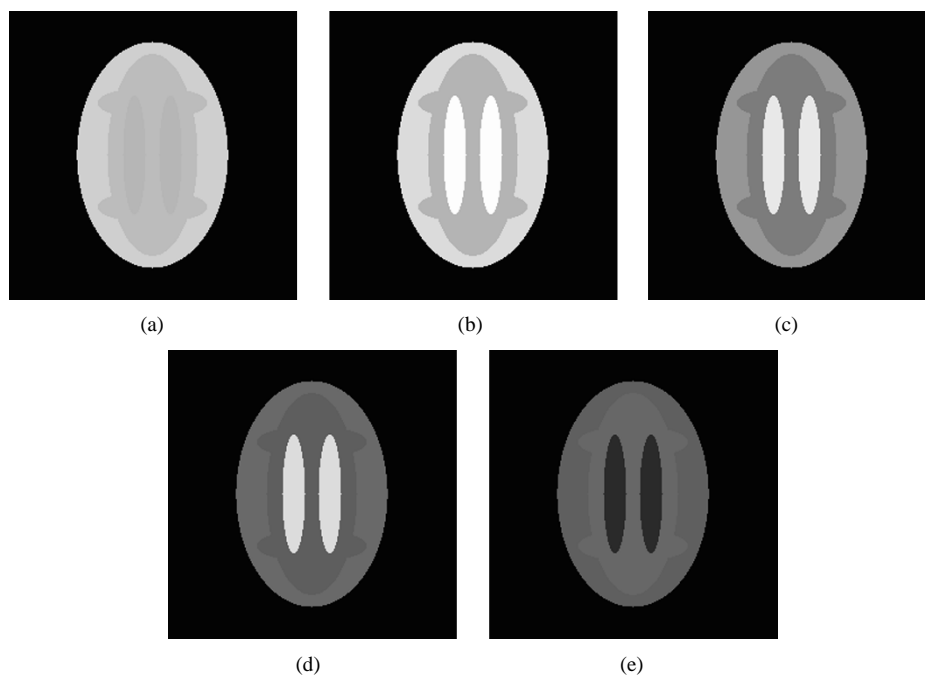
Fig. 1. Five band test phantoms for simulation study. (a) Band 1. (b) Band 2. (c) Band 3. (d) Band 4. (e) Band 5.

IV. EXPERIMENTAL RESULTS

In this section, we present two sets of experiments, one set of computer-generated phantom images and another set of real magnetic resonance images. The phantom image experiments enable us to conduct a quantitative study and error analysis for the CEM approach while the real MRI experiments allow us to assess its utility and effectiveness in medical diagnosis.

A. Computer Simulations for Phantom Experiments

In this section, a series of computer simulations is performed to conduct a quantitative study and performance analysis of the CEM approach in comparison with the CM method described in Section III with number of classes $c = 4$ representing four classes of WM, GM, CSF, and image background. The computer-generated phantom images used for simulations are shown in Fig. 1 which have five bands, each of which was made up of six overlapped ellipses with their radiance spectral signatures shown in Fig. 2. These ellipses represent structure areas of three interesting cerebral tissues corresponding to gray matter (GM), white matter (WM), and cerebral spinal fluid (CSF). From the periphery to the center are background (BKG), GM, WM, and CSF simulated by the signatures given in Fig. 2. The gray level values of these areas in each band were simulated in such a fashion that these values reflect the average values of their respective tissues in real MR images shown in Fig. 4. Table I tabulates the values of the parameters used by the MRI pulse sequence and the gray level values of the tissues of each band used in the experiments. A zero-mean Gaussian noise was added to the phantom images in Fig. 1 so as to achieve different levels of signal-to-noise ratios (SNRs) ranging from 5 dB to 20 dB. Despite the fact that such MR phantom images may be unrealistic, they only serve as a purpose for illustration of the proposed CEM technique and demonstration of its advantages.
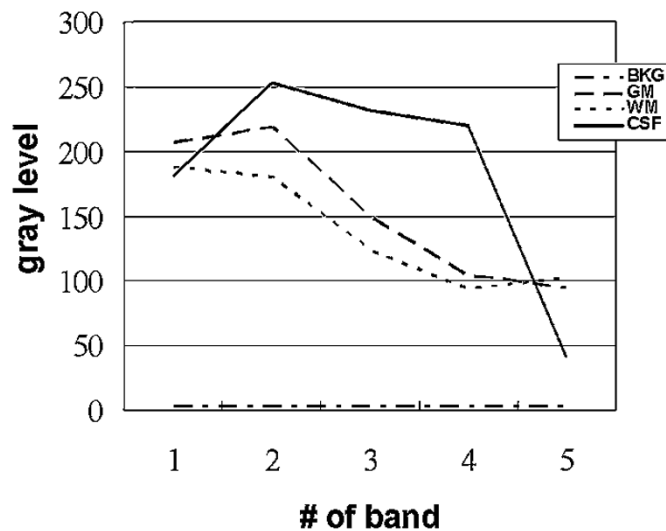
Fig. 2. GM, WM, CSF, and BKG spectral signatures.

TABLE I
VALUES OF THE PARAMETERS USED BY THE MRI PULSE SEQUENCE
AND THE GRAY LEVEL VALUES OF THE TISSUES OF
EACH BAND USED IN THE EXPERIMENTS

Band #	MRI Parameter	GM	WM	CSF
Band 1	TR/TE=2500ms/25ms	207	188	182
Band 2	TR/TE=2500ms/50ms	219	180	253
Band 3	TR/TE=2500ms/75ms	150	124	232
Band 4	TR/TE=2500ms/100ms	105	94	220
Band 5	TR/TE=500ms/11.9ms	95	103	42

1) Abundance Percentage Thresholding Method: In order to apply the CEM filter to these phantom images, the desired object signature **d** was specified by one of three objects of our interest, GM, WM, and CSF whose spectral signatures are shown in Fig. 2. As noted previously, the images generated

Fig. 3.   ROC curves generated by CEM with SNR $= 5, 10, 15,$ and 20 dB. (a) Three-dimensional ROC curves of $(R_D, R_F\ a\%)$. (b) Two-dimensional ROC curves of (R_D, R_F). (c) Two-dimensional curves of $(R_D, a\%)$. (d) Two-dimensional curves of $(R_F, a\%)$.
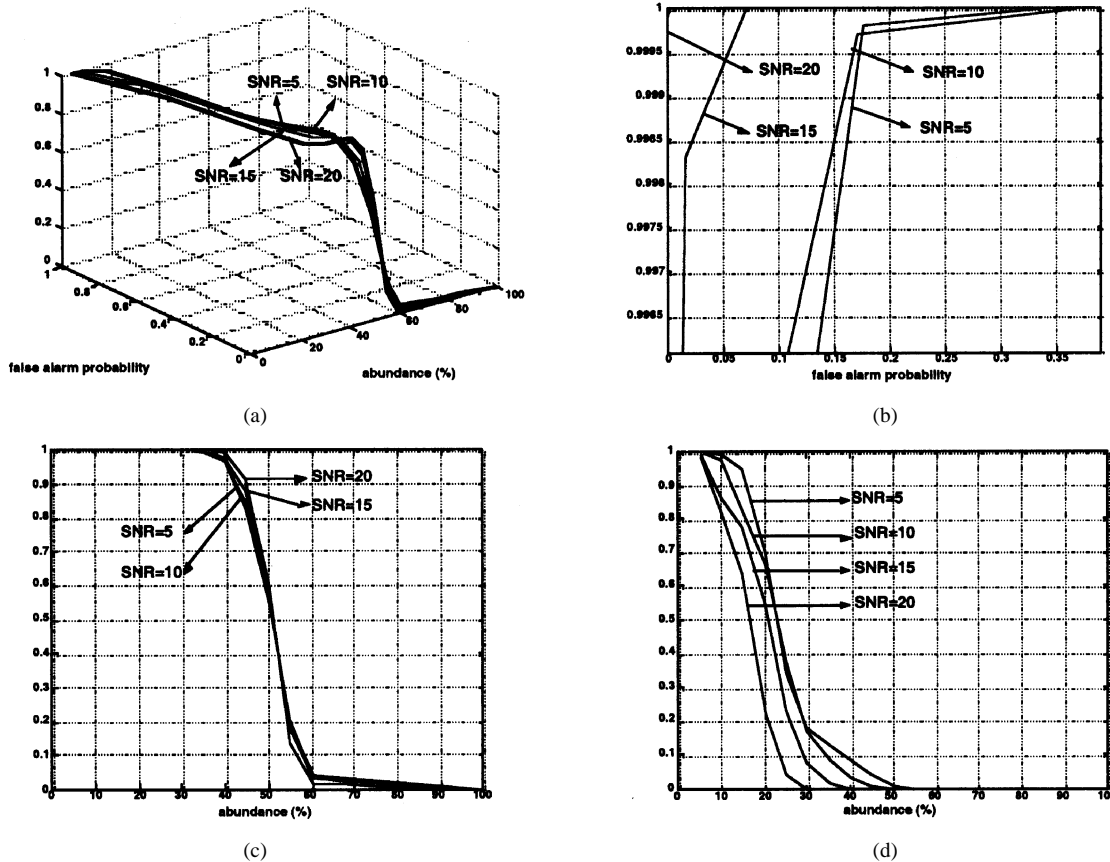
by the CEM filter were gray scale with the gray level values proportional to detected abundance fraction of $\mathbf{d}$. On the other hand, the CM method is a classical class-label process which assigns each data sample vector to one and only one class. So, the CM-generated image is a classification map rather than a gray scale image as generated by the CEM filter. In order to conduct a quantitative study and compare with the results produced by the CM method, we convert the CEM-generated abundance fractional images to binary images. Here, we adopt an approach proposed in [31], which used the abundance fraction percentage as a cutoff threshold value for such conversion. We first normalize the abundance fractions of all the pixels in a CEM-generated abundance fractional image to the range of $[0, 1]$. More specifically, let $\mathbf{r}$ be the image pixel vector and $\hat{\alpha}_1(\mathbf{r}), \hat{\alpha}_2(\mathbf{r}), \ldots, \hat{\alpha}_p(\mathbf{r})$ are the estimates of the abundance fractions, $\alpha_1, \alpha_2, \ldots, \alpha_p$ present in the $\mathbf{r}$ that are produced by applying the CEM in (5) to the image pixel vector $\mathbf{r}$. Then for each estimated abundance fraction $\hat{\alpha}_j(\mathbf{r})$ its normalized abundance fraction, $\tilde{\alpha}_j(\mathbf{r})$ can be obtained by

$$\tilde{\alpha}_j(\mathbf{r}) = \frac{\hat{\alpha}_j(\mathbf{r}) - \min_{\mathbf{r}} \hat{\alpha}_j(\mathbf{r})}{\max_{\mathbf{r}} \hat{\alpha}_j(\mathbf{r}) - \min_{\mathbf{r}} \hat{\alpha}_j(\mathbf{r})}. \qquad (6)$$

Suppose that $a\%$ is used for the cutoff abundance fraction threshold value. If the normalized abundance fraction of a pixel is greater than or equal to $a\%$, then the pixel is detected as the desired object pixel and assigned by a "1"; otherwise, the pixel

is assigned by a "0", in which case the pixel does not match the desired object signature $\mathbf{d}$. Using this thresholding criterion, we can actually tally the number of pixels that the CEM filter detected in its generated abundance fractional images and further develop a three-dimensional (3-D) receiver operating characteristic (ROC) analysis based on $a\%$.

2) Three-Dimensional ROC Analysis: First of all, let $\{\mathbf{d}_i\}_{i=1}^p$ be a set of objects of interest, which we would like to classify. We define $N(\mathbf{d}_i)$, $N_D(\mathbf{d}_i)$, and $N_F(\mathbf{d}_i)$ to be the total number of pixels specified by the ith object signature $\mathbf{d}_i$, the total number of pixels that are specified by the object signature $\mathbf{d}_i$ and actually detected as the $\mathbf{d}_i$ by the CEM filter, and the total number of false alarm pixels that are not specified by the object signature $\mathbf{d}_i$ but detected as the $\mathbf{d}_i$ by the CEM filter, respectively. For example, the desired object signature $\mathbf{d}_i$ can be chosen to be one of GM, WM, or CSF. Using the definitions of $N(\mathbf{d}_i)$, $N_D(\mathbf{d}_i)$, and $R_F(\mathbf{d}_i)$ we further define the detection rate $R_D(\mathbf{d}_i)$, false alarm rate $R_F(\mathbf{d}_i)$ for $\mathbf{d}_i$, mean detection rate R_D, and mean false alarm rate R_F by

$$R_D(\mathbf{d}_i) = \frac{N_D(\mathbf{d}_i)}{N(\mathbf{d}_i)} \qquad (7)$$

$$R_F(\mathbf{d}_i) = \frac{N_F(\mathbf{d}_i)}{N - N(\mathbf{d}_i)} \qquad (8)$$

$$R_D = \sum_{i=1}^p R_D(\mathbf{d}_i) p(\mathbf{d}_i) \qquad (9)$$

$$R_F = \sum_{i=1}^{p} R_F(\mathbf{d}_i)p(\mathbf{d}_i) \qquad (10)$$

where N is the total number of pixels in the image and $p(\mathbf{d}_i) = N(\mathbf{d}_i)/\sum_{i=1}^{p} N(\mathbf{d}_i)$. It is worth noting that the mean detection rate R_D defined by (9) is the mean of detection rates over the detected objects. This is because the CEM filter detects one object at a time. In order to classify p objects $\{\mathbf{d}_i\}_{i=1}^{p}$, the CEM filter must be performed p times and calculate its mean detection rate. Similarly, the mean false alarm R_F defined by (10) is the mean of false alarm rates over the detected objects. Using (7)–(10), each fixed $a\%$ produces a pair of R_D and R_F. As a consequence, varying $a\%$ from 0% up to 100% generates a set of pairs (R_D, R_F) where each pair results from a particular $a\%$ being used as a cutoff threshold value. In this case, we use an approach proposed in [32] to plot a 3-D ROC curve based on three parameters, $(R_D, R_F, a\%)$, where the (x, y) coordinate corresponds $(R_F, a\%)$ and z axis is specified by R_D. By means of such a 3-D ROC curve we can further plot three two-dimensional (2-D) curves of (R_D, R_F), $(R_D, a\%)$, and $(R_F, a\%)$ where the 2-D curve of (R_D, R_F) can be viewed as the traditional ROC curve in [33]. Now we can use this 3-D ROC curve along with three 2-D curves to analyze the performance of the CEM filter with different SNRs in detection of GM, WM, and CSF. Fig. 3(a)-(b) plots its 3-D ROC curves of $(R_D, R_F, a\%)$ and 2-D curves of (R_D, R_F), $(R_D, a\%)$, and $(R_F, a\%)$ for SNR = 5, 10, 15, and 20 dB, respectively. The 3-D ROC curves in Fig. 3(a) show the performance of a classifier as a function of three parameters R_D, R_F, and $a\%$, while the 2-D curves of (R_D, R_F) in Fig. 3(b) provide the mean detection rate of a classifier versus the mean false alarm rate. It should be noted that the 2-D curves of (R_D, R_F) in Fig. 3(b) were plotted in the ranges of $R_D = [0.9965, 1]$ and $R_F = [0, 0.4]$ for visual inspection. According to the 2-D curves in Fig. 3(b), the CEM filter performed extremely well when SNR = 15 and 20 dB. Then, its performance was degraded when SNR was decreased. Additionally, the 2-D curves of $(R_D, a\%)$ and $(R_F, a\%)$ in Fig. 3(c)-(d) indicate how a threshold value of $a\%$ affects the performance of a classifier. Fig. 3(c) shows that the CEM filter with four different SNRs performed similarly when their R_D began to drop gradually starting at $a\% = 30\%$, then rapidly between 45% and 55% and finally close to zero after 60%. Fig. 3(d) also demonstrates similar results but the differences among these four SNRs were more visible. It clearly shows that the R_F of the CEM filter with SNR = 20 dB dropped rapidly between $a\% = 5\%$ and 25% and reached zero around $a\% = 30\%$. The R_F of the CEM filter with SNR = 5 dB also dropped rapidly from $a\% = 15\%$ to 30% and reached zero around $a\% = 50\%$. The R_F of the CEM filter with SNR = 10 and 15 dB was somewhere between these two curves. From Fig. 3(c)-(d), we can see that a good compromise of $a\%$ for SNR = 20 between R_D and R_F was around 25%, 30% for SNR = 15 dB and 35% for SNR = 10 dB and 5 dB. This was further justified by the classification results of GM, WM, and CSF for the cases of SNR = 5 dB in Table II and 20 dB in Table III where the cutoff threshold value of $a\%$ was chosen to be 5%, 20%, 25%, 30%, 35%, 40%, 45%, and 50%. Table IV also tabulated the classification results of the CM method for comparison. As we can see, the CEM performed

TABLE II
CLASSIFICATION RESULTS OF GM, WM, AND CSF FOR THE CASE OF SNR = 5 dB WHERE THE CUTOFF THRESHOLD VALUE OF $a\%$ WAS CHOSEN TO BE 5%, 20%, 25%, 30%, 35%, 40%, 45%, AND 50%

	$a\%$	$N(\mathbf{d})$	$N_D(\mathbf{d})$	$N_F(\mathbf{d})$	$R_D(\mathbf{d})\%$	$R_F(\mathbf{d})\%$
GM	5%	9040	9040	56473	100.00	99.96
	20%	9040	9040	36363	100.00	64.36
	25%	9040	9040	14584	100.00	25.81
	30%	9040	9037	11131	99.97	19.70
	35%	9040	8977	8997	99.30	15.93
	40%	9040	8611	5948	95.25	10.53
	45%	9040	7090	2751	78.43	4.87
	50%	9040	4281	707	47.36	1.25
WM	5%	8745	8745	56779	100.00	99.98
	20%	8745	8745	51235	100.00	90.22
	25%	8745	8745	31149	100.00	54.85
	30%	8745	8744	12697	99.99	22.36
	35%	8745	8712	8036	99.62	14.15
	40%	8745	8425	5479	96.34	9.65
	45%	8745	7092	2405	81.10	4.23
	50%	8745	4427	591	50.62	1.04
CSF	5%	3282	3282	62223	100.00	99.95
	20%	3282	3282	20581	100.00	33.06
	25%	3282	3282	2302	100.00	3.70
	30%	3282	3282	115	100.00	0.18
	35%	3282	3282	1	100.00	0.00
	40%	3282	3282	0	100.00	0.00
	45%	3282	3247	0	98.93	0.00
	50%	3282	2749	0	83.76	0.00

TABLE III
CLASSIFICATION RESULTS OF GM, WM AND CSF FOR THE CASE OF SNR = 20 dB WHERE THE CUTOFF THRESHOLD VALUE OF $a\%$ WAS CHOSEN TO BE 5%, 10%, 15%, 20%, 25%, 30%, 35%, 40%, 45%, AND 50%

	$a\%$	$N(\mathbf{d})$	$N_D(\mathbf{d})$	$N_F(\mathbf{d})$	$R_D(\mathbf{d})\%$	$R_F(\mathbf{d})\%$
GM	5%	9040	9040	56429	100.00	99.88
	20%	9040	9040	14067	100.00	24.90
	25%	9040	9040	3658	100.00	6.47
	30%	9040	9040	498	100.00	0.88
	35%	9040	9039	19	99.99	0.03
	40%	9040	9013	0	99.70	0.00
	45%	9040	8520	0	94.25	0.00
	50%	9040	5966	0	66.00	0.00
WM	5%	8745	8745	56725	100.00	99.88
	20%	8745	8745	15489	100.00	27.27
	25%	8745	8745	1736	100.00	3.06
	30%	8745	8745	60	100.00	0.11
	35%	8745	8745	2	99.98	0.00
	40%	8745	8745	0	99.88	0.00
	45%	8745	8745	0	85.42	0.00
	50%	8745	3774	0	43.16	0.00
CSF	5%	3282	3282	57137	100.00	91.78
	20%	3282	3282	0	100.00	0.00
	25%	3282	3282	0	100.00	0.00
	30%	3282	3282	0	100.00	0.00
	35%	3282	3282	0	100.00	0.00
	40%	3282	3282	0	100.00	0.00
	45%	3282	3282	0	100.00	0.00
	50%	3282	2849	0	86.81	0.00

considerably better than the CM method when the cutoff threshold value $a\%$ chosen from the range of 25%–35%.

Since 2-D curves of (R_D, R_F) is similar to the 2-D ROC curve commonly used in detection theory, we can calculate the area under the 2-D curve of (R_D, R_F) [33] to quantitatively study the overall performance of the CEM filter. The first row of Table V tabulates the mean detection rates calculated from
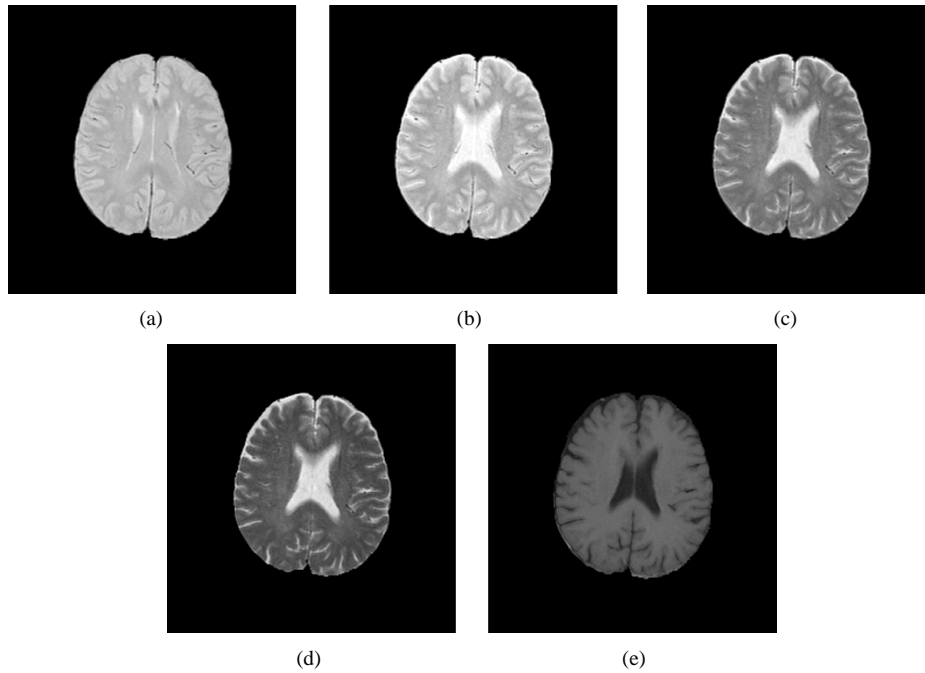
(a)   (b)   (c)

(d)   (e)

Fig. 4. Five spectral bands of real MR brain images. (a) TR/TE $= 2500$ ms/25 ms. (b) TR/TE $= 2500$ ms/50 ms. (c) TR/TE $= 2500$ ms/75 ms. (d) TR/TE $= 2500$ ms/100 ms (e) TR/TE $= 500$ ms/11.9 ms

TABLE IV
CLASSIFICATION RESULTS OF GM, WM AND CSF FOR CM METHOD
FOR SNR $= 5$ AND 20 dB

	SNR	N(**d**)	N$_D$(**d**)	N$_F$(**d**)	R$_D$(**d**)%	R$_F$(**d**)%
GM	5dB	9040	8708	6277	96.33	11.11
	20dB	9040	9040	7489	100.00	13.26
WM	5dB	8745	8517	6201	97.39	10.92
	20dB	8745	8745	9285	100.00	16.35
CSF	5dB	3282	2941	4003	89.61	6.43
	20dB	3282	3166	4001	96.47	6.43

TABLE V
MEAN DETECTION RATES CALCULATED FROM THE 2-D CURVES OF (R_D, R_F)
IN FIG. 3(b) AND CLASSIFICATION RATES PRODUCED BY THE CM METHOD

	SNR = 5dB	SNR = 10dB	SNR = 15dB	SNR = 20dB
CEM	0.9786	0.9930	1.0000	1.0000
CM method	0.9572	0.9845	0.9889	0.9945

(a)   (b)

(c)

Fig. 5. Classification results produced by the CEM using the five images in Fig. 4; (a) GM, (b) WM, (c) CSF.

the areas under 2-D curves of (R_D, R_F) in Fig. 3(b) where the CEM performance was steadily improved as SNR was increased. In order to evaluate the CEM performance against the CM method, the second row of Table V tabulates the results of the CM method for SNR $= 5, 10, 15,$ and 20. It should be noted that no ROC curves can be generated by the CM method since the CM method is a labeling process and each SNR results in a fixed point specified by one and only one pair (R_D, R_F). As shown in Table V, the overall performance of the CEM filter is only slightly better than the CM method. This is because the mean detection rate for the CEM filter was calculated for $a\%$ ranging from 0% to 100% and the CEM performance was considerably offset by the poor performance yielded by $a\%$ after 35% as demonstrated in Tables II and III for $a\% = 40\%, 45\%,$ and 50%.
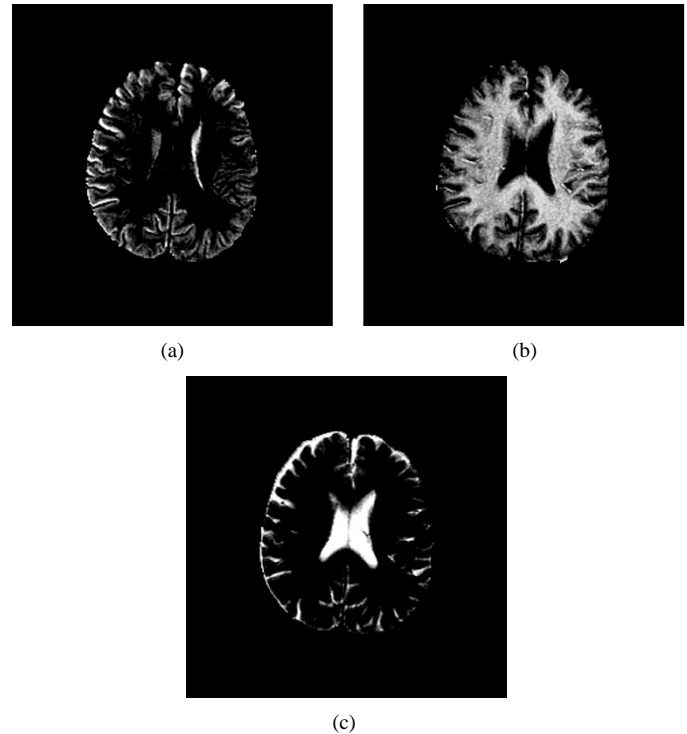
B. Real MR Image Experiments

In the following experiments, real MR images were used for performance evaluation. They were acquired from ten patients with normal physiology and no intensity inhomogeneity correct method was applied to the MR image data. The MR images to be studied for our experiments are shown
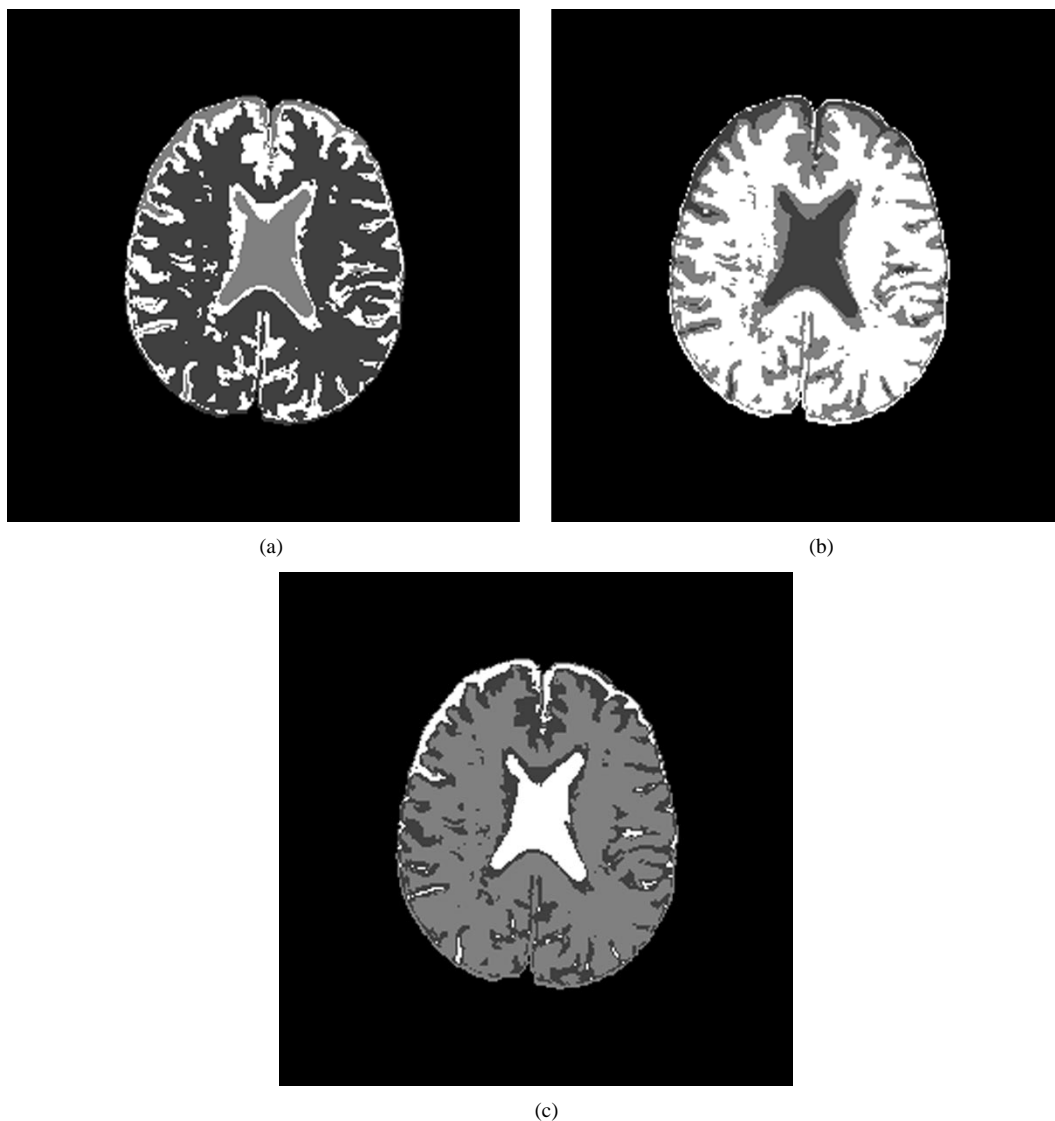
Fig. 6. Classification results produced by the CM method using the five images in Fig. 4. (a) GM = 255, CFS = 128, WM = 64, and BKG = 0. (b) WM = 255, GM = 128, CSF = 64, and BKG = 0. (c) CSF = 255, WM = 128, GM = 64, and BKG = 0.

in Fig. 4(a)–(e) with the same parameter values in Table I. Band 1 is the PD-weighted spectral image acquired by the pulse sequence TR/TE = 2500 ms/25 ms. Bands 2, 3, and 4 are T2-weighted spectral images were acquired by the pulse sequences TR/TE = 2500 ms/50 ms, TR/TE = 2500 ms/75 ms, and TR/TE = 2500 ms/100 ms, respectively. Band 5 is the T1-weighted spectral image acquired by the pulse sequence TR/TE = 500 ms/11.9 ms. The tissues surrounding the brain such as bone, fat, skin, were semiautomatically extracted using interactive thresholding and masking [34]. The slice thickness of all the MR images are 6 mm and axial section were taken from GE MR 1.5T scanner. Before acquisition of the MR images the scanner was adjusted to prevent artifacts caused by the magnetic field of static, radio-frequency and gradient. All experiments presented in this paper were performed under supervision of and verified by experienced neuroradiologists.

In many MRI applications, the three cerebral tissues, GM, WM, and CSF, are of major interest where their knowledge can be generally obtained directly from the images. In our experiments, the spectral signatures of GM, WM, and CSF used for

the CEM were extracted directly from the MR images and verified by experienced radiologists. Following the same manner conducted for MR phantom image experiments, we used five images in Fig. 4(a)–(e) with the desired object signatures specified in Fig. 2. Fig. 5(a)–(c) shows the detection results of the CEM filter for GM, WM, and CSF where the images labeled by (a), (b) and (c) were produced, respectively, by the CEM filter using GM, WM, and CSF as desired object signatures $\mathbf{d}$. For comparison, we also applied the CM method to Fig. 4(a)–(e) to produce Fig. 6(a)–(c) with the number of classes, $c = 4$ to represent four classes, GM, WM, CSF, and image background where the detection results of GM, WM, and CSF are labeled by (a), (b), and (c), respectively. As noted, the CM method was not stable due to its nature in unsupervised learning. When each time the CM method was implemented, a different classification map was generated. The results in Fig. 6 were obtained by averaging five runs of implementation of the CM method. Note that the CM method proposed in Section III is slightly different from the commonly used CM method, which does not designate any object signature as a specific pattern class. In the

implementation of our proposed CM method, the desired object signature was designated as one specific class and this class was fixed during its unsupervised clustering. This is because the CEM required the knowledge of the desired object signatures. In order to make a fair comparison between the CM method and the CEM, the information of the desired object signatures required for the CEM was also made available to the CM method. As a result, three images [Fig. 6(a)–(c)] were 4-class classification maps with GM, WM, and CSF designated as desired object signatures, respectively. For example, in the classification map of Fig. 6(a) the GM signature in Fig. 2 was used as the desired signature in the initial step of the CM method with $p = 1$ and $\mathbf{d}_1 =$ GM where the pixels classified into the GM class were assigned to be highest gray level value 255 and the pixels in the CSF class, WM class and background class were assigned to 128, 64, and 0, respectively. Similarly, the classification maps of Fig. 6(b)-(c) were obtained by assigning the gray level value 0 to the background and the gray level value 255 to the pixels classified in the WM and CSF, respectively, while in Fig. 6(b) the gray level values 128 and 64 assigned to the pixels falling in the GM and CSF classes, respectively, and in Fig. 6(c) the gray level values 128 and 64 assigned to the pixels belonging to the WM and GM classes, respectively. The gray level values assigned to these four classes for each case were a purely empirical choice to maximize the contrast of the desired object signature.

As for computational complexity, we used Pentium III, 733-Mhz PCs to run all the experiments for the CEM and our CM method. It was found that the CEM produced one detection image almost instantly with less than a second (865 ms). Compared with the CEM, the CM method required about 4 min. (248 021 ms) for each run to generate one classification map. Since the CM method needed 5 runs of the CM method to obtain the average performance for each case of using GM, WM, and CSF as the desired object signatures, a total of 15 runs was required to generate the three images in Fig. 6(a)–(c) with computing time of about one hour.

In MR phantom image experiments, Gaussian noise was simulated to achieve various SNR for quantitative analysis. Unfortunately, a quantitative study will be difficult for the above real MR image experiments for the following two reasons. One is that it requires reliable techniques to estimate noise in the MR images. This has been a challenging issue in signal and image processing [35], [36] and beyond the scope of this paper. The CEM filter generates gray scale abundance fractional images for MR image classification which provide radiologists with gray level information for their visual interpretation. Such qualitative information is useful for medical diagnosis, but will be lost if gray scale images are converted to binary images by thresholding. In addition, it is nearly impossible for radiologists to identify all the pixels in real MR images for quantitative study as the way we did for phantom images where we knew exactly what class to which each pixel belonged. As a consequence, no quantitative analysis was conducted for the real MR image experiments.

C. Discussion and Conclusion

The CEM is a new technique, which recently showed great success in remote sensing image classification [37]. It considers
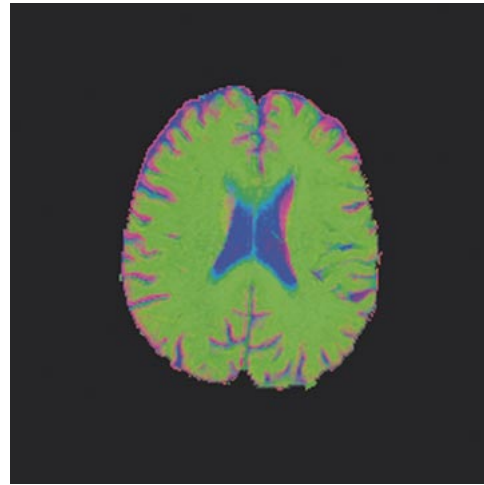

Fig. 7. An R–G–B color image fused by the three images in Fig. 5(a)–(c).

a pixel as a mixture of object signatures present in the image data and unmixes the object signature by estimating their abundance fractions resident in the pixel. As a result, it produces a gray scale abundance fractional image for each object signature with gray level values proportional to the abundance fractions of the object signature contained in the pixel. Its detection and classification is then performed by these generated abundance fractional images. Such analysis is referred to as subpixel detection and mixed pixel classification in remote sensing literature. Compared with traditional spatial-based image classification techniques that are basically class-label assignment processes on the basis of pure pixels, the CEM is actually an estimation technique operating on mixed pixels. Consequently, the performance of the CEM is determined by three parameters: detection rate, R_D; false alarm rate, R_F; and abundance fraction, $a\%$. In order to evaluate the inter-relationship among these parameters, a new 3-D ROC analysis was proposed in Section IV-A and used for performance evaluation for phantom image experiments. The concept of such a 3-D ROC analysis was recently developed for hyperspectral image analysis [38], [39]. The 2-D ROC analysis is well established for signal detection theory, which is based on testing two hypotheses. However, the proposed 3-D ROC analysis is developed for signal estimation theory which is based on signal abundance fractions estimated from the data with the third dimension specified by abundance fraction, $a\%$. When a particular value of $a\%$ is used to threshold a gray scale abundance fractional image into a binary image, it results in a pair of (R_D, R_F) that corresponds to a point in a 2-D ROC curve. So, the 3-D ROC curve is still a one-dimensional curve, not a 3-D surface. It can only be described in a 3-D space formed by three parameters $(R_D, R_F, a\%)$ where each point on the 3-D curve is a result of a pair of (R_D, R_F) with a specific $a\%$ used as a cutoff threshold value. As noted, when the threshold value of $a\%$ is set too low, a mixed pixel may contain more than one object signature whose abundance fraction exceeds the threshold value $a\%$. Consequently, the pixel may be classified to more than one class. If the $a\%$ is set too high, a pixel must have a sufficiently enough abundance fraction to be declared as a target. Otherwise, the pixel will be assigned to a background pixel. Such scenarios
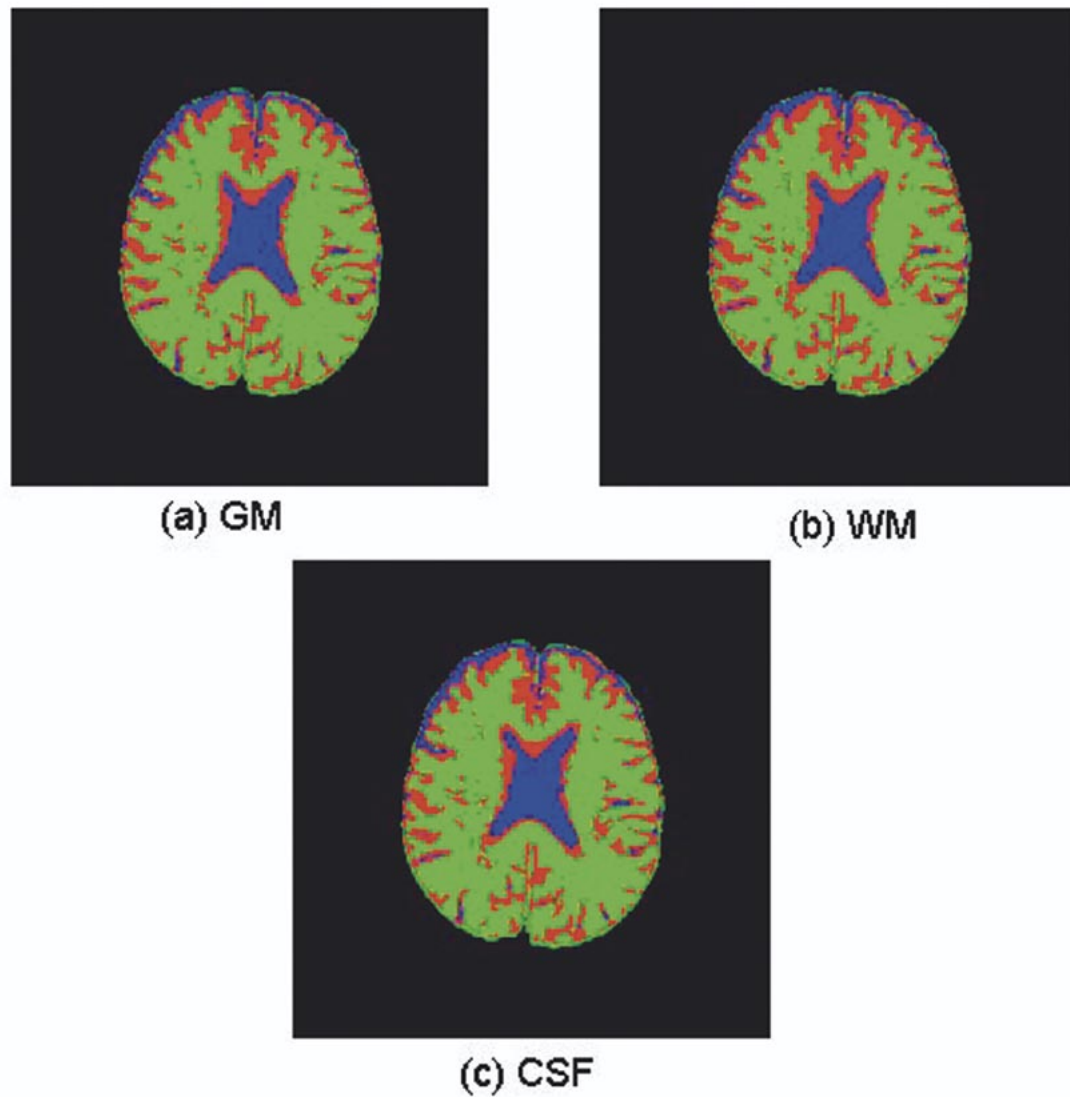
Fig. 8. Three R–G–B color images produced for each of Fig. 6(a)–(c); (a) GM, (b) WM, (c) CSF.

will occur in mixed pixel classification, but not in pure pixel classification.

Since the CEM designates a particular object signature as a desired target signature for detection, it must perform for each object signature to achieve classification as demonstrated in Fig. 5. However, its classification can be also performed by fusing all separate detected objects into one image by assigning different colors to distinct detected objects. Fig. 8 shows a color image that used red, green and blue to represent GM, WM, and CSF, respectively, for visualization. As shown in [38]–[40], this image fusion can be done by extending the CEM to a linearly constrained minimum variance approach that can simultaneously classify multiple object signatures using different colors to highlight detected objects. The color of a mixed pixel is mixed by colors assigned to the object signatures that are present in the pixel. So, the mixture of colors in a mixed pixel indicates how various object signatures are mixed with different abundance fractions. For an

extreme case, an equal R–G–B mixed color will be white. The advantage of using color visualization cannot be gained by traditional spatial-based classification methods such as the CM method. As a comparative example, we also produced three R–G–B color images in Fig. 8(a)–(c) for the three images in Fig. 6(a)–(c) which adopted the same color assignment used for the CEM-generated image (i.e., red for GM, green for WM, and blue for CSF). As we can see from Fig. 8, there is no visible difference among the three-color images produced by the three detection images in Fig. 6(a)–(c). More importantly, the three color were distinct and no mixed colors were found in the images. This is not true for Fig. 7. As we compare Fig. 8 with Fig. 7, the CEM-generated color image provides mixture information of the three tissue signatures via their mixing colors, whereas the colors of the three images in Fig. 8(a)–(c) are simply pure not mixed.

Another advantage of the CEM is computational efficient. As noted in our experiments, it took less than one second to gen-

erate one image result. Compared with the CM method that required about 3 min, it was a tremendous saving. Most of all, the significant strength resulting from the CEM is that it does not require background knowledge. In particular, the CEM suppresses the image background while it extracting the desired object signature. There is no need for the CEM to classify the image background into different pattern classes. This advantage is particularly useful when the image background is complicated and difficult to characterize.

As a concluding remark, the CM method proposed in Section III takes advantage of the knowledge of desired object signatures in its clustering process. Should this knowledge not be used, our proposed CM method would have become the commonly used unsupervised CM method. In this case, all the cluster centers must be reshuffled each time when the clustering is performed because the desired object signatures might not be cluster centers as we wish. The resulting performance may not be as good as our proposed CM method. Besides, it may also require extra computing time to cluster an additional class due to the fact that there is no fixed cluster center designated for a desired object signature.

V. Conclusion

This paper presents a new spectral-based technique to MR image classification, CEM. Three major results are contributed to this paper. In classical pattern classification, the data are required to be classified into a number of pattern classes. However, when it is applied to real data, there is a major issue generally involved, which is how to deal with background. In many practical applications, what we are interested is object classification rather than background classification. Besides, classifying background could be very challenging since the background is usually not unknown. By working on real data without prior knowledge about background, there is no way to know if background classification will faithfully reflect the real data. On the other hand, in many situations, we generally have prior knowledge about the objects in which we are interested. So, one contribution of the proposed CEM method is that it remedies this problem. It can extract the objects of interest while effectively minimizing interfering effects resulting from unknown signal sources which include background sources. In medical images, the object to be classified are generally human tissues which are soft objects. In general, these soft tissues have deformable shapes and cannot be effectively analyzed by classical spatial-based techniques that primarily designed for rigid object recognition such as vehicles, industrial tools, etc. Therefore, a second contribution of this paper is that the CEM views an MR image sequence as a multispectral image cube with each pixel represented by a spectral pixel vector. By considering the image cube as a whole, the CEM takes advantage of spectral properties present in each pixel vector as well as spectral correlation among sample pixel vectors. This benefit certainly cannot be gained by any spatial-based image analysis techniques. A third contribution made in this paper is a new approach to 3-D ROC analysis, which is based on three parameters, detection probability, false alarm probability, and abundance percentage. As we know,

the classification results produced by classical spatial-based pattern classification techniques are basically classification maps, which show labels of each pixel. By contrast, the image produced by the CEM filter is essentially a gray scale image. In order to evaluate its performance, the classical 2-D ROC analysis is extended to a 3-D ROC analysis which is based on three parameters, detection rate, false alarm rate, and abundance fraction percentage. Including object abundance fractions as a third dimension in ROC curves is particularly useful for spectral imagery where spectral information can be characterized separated from spatial information.

References

[1] G. A. Wright, "Magnetic resonance image," *IEEE Signal Processing Mag.*, pp. 56–66, Jan. 1997.

[2] G. Sebastiani and P. Barone, "Mathematical principles of basic magnetic resonance image in medicine," *Signal Process*, vol. 25, pp. 227–250, 1991.

[3] B. Johnston, M. S. Atkins, B. Mackiewich, and M. Anderson, "Segmentation of multiple sclerosis lesions in intensity corrected multispectral MRI," *IEEE Trans. Med. Imag.*, vol. 15, pp. 154–169, Apr. 1996.

[4] A. P. Dhawan, A. Zavaljevski, A. Sarwal, and W. S. Ball, "A system for MR brain image segmentation," in *Proc. 18th Annu. Int. Conf. IEEE Engineering in Medicine and Biology Society*, Amsterdam, The Netherlands, 1996, pp. 732–733.

[5] L. Verard, J. Fadidi, S. Ruan, and D. Bloyet, "3D MRI segmentation of brain structures," in *Proc. 18th Annu. Int. Conf. IEEE Engineering in Medicine and Biology Society*, Amsterdam, The Netherlands, 1996, pp. 1081–1082.

[6] H. Grahn, N. M. Szeverenyi, N. W. Roggenbuck, F. Delaglio, and P. Geladi, "Data analysis of multivariate magnetic resonance images I. A principal component analysis approach," *Chemometrics Intell. Lab. Syst.*, vol. 5, pp. 11–322, 1989.

[7] J. P. Windham, M. A. Abd-Allah, D. A. Reimann, J. W. Froehich, and A. M. Haggar, "Eigneimage filtering in MR imaging," *J. Comput. Assist. Tomogr.*, vol. 12, no. 1, pp. 1–9, Jan./Feb. 1988.

[8] H. Soltanian-Zadeh and J. P. Windham, "Novel and general approach to linear filter designed for contrast-to-noise ratio enhancement of magnetic resonance images with multiple interfering features in the scene," *J. Electron. Imag.*, vol. 1, no. 2, pp. 171–182, Apr. 1992.

[9] A. M. Haggar, J. P. Windham, D. A. Reimann, D. C. Hearshen, and J. W. Froehich, "Eigneimage filtering in MR imagine: An application in the abnormal chest wall," *Magn. Reson. Med.*, vol. 11, pp. 85–97, 1989.

[10] H. Soltanian-Zadeh, J. P. Windham, H. Soltanian-Zadeh, J. P. Windham, and A. E. Yagle, "A comparative analysis of several transformations for enhancement and segmentation of magnetic resonance image scene sequences," *IEEE Trans. Med. Imag.*, vol. 11, pp. 302–316, Sept. 1992.

[11] H. Soltantian-Zadeh, R. Saigal, A. M. Haggar, J. P. Windham, A. E. Yagle, and D. C. Hearshen, "Optimization of MRI protocola and pulse sequence parameters for eigneimage filtering," *IEEE Trans. Med. Imag.*, vol. 13, pp. 161–175, Mar. 1994.

[12] H. Soltanian-Zadeh, J. P. Windham, and D. J. Peck, "Optimal linear transformation for MRI feature extraction," *IEEE Trans. Med. Imag.*, vol. 15, pp. 749–767, Dec. 1996.

[13] W. E. Reddick, J. O. Glass, E. N. Cook, T. D. Elkin, and R. J. Deaton, "Automated segmentation and classification of multispectral magnetic resonance images of brain using artificial neural networks," *IEEE Trans. Med. Imag.*, vol. 16, pp. 911–918, Dec. 1997.

[14] J. Alirezaie, M. E. Jernigan, and C. Nahmias, "Automatic segmentation of cerebral MR images using artificial neural networks," *IEEE Trans. Nucl. Sci.*, vol. 45, no. 4, pp. 2174–2182, August 1998.

[15] J. S. Lin, R. M. Chen, and Y. M. Huang, "Medical image sementation using field annealing network," in *Proc. IEEE Int. Conf. Image Processing*, vol. 2, Oct. 1997, pp. 855–858.

[16] J. S. Lin, K. S. Cheng, and C. W. Mao, "Multispectral magnetic resonance images segmentation using fuzzy Hopfield neural network," *Int. J. Biomed. Computing*, pp. 205–214, Aug. 1996.

[17] ——, "Modified Hopfied neural network with fuzzy *c*-means technique for multispectral MR image segmentation," in *Proc. IEEE Int. Conf. Image Processing*, vol. 1, Sept. 1996, pp. 327–330.

[18] M. C. Clark, L. O. Hall, D. B. Goldof, L. P. Clarke, R. P. Velthuizen, and M. S. Sibiger, "MRI segmentation using fuzzy clustering techniques," *IEEE Eng. Med. Biol. Mag.*, pp. 730–742, Nov./Dec. 1994.

[19] M. S. Atkins and B. T. Mackiewich, "Fully automatic segmentation of brain in MRI," *IEEE Trans. Med. Imag.*, vol. 17, pp. 98–107, Feb. 1998.

[20] M. C. Clark, L. O. Hall, D. B. Goldof, R. Velthuizen, F. R. Murtagh, and S. Silbiger, "Automatic tumor segmentation using knowledge-based techniques," *IEEE Trans. Med. Imag.*, vol. 17, pp. 187–201, Apr. 1998.

[21] C.-M. Wang, S.-T. Yang, P.-C. Chung, C. S. Lo, C.-I. Chang, C. C. Chen, C.-W. Yang, and C. H. Wen, "Orthogonal subspace projection-based approaches to classification of MR image sequences," Computerized Med. Imag. Graphics, to be published.

[22] J. C. Harsanyi, "Detection and classification of subpixel spectral signatures in hyperspectral image sequences," Ph.D. dissertation, Dept, Elect. Eng., Univ. Maryland Baltimore County, Baltimore, MD, 1993.

[23] J. C. Harsanyi, W. Farrand, and C.-I. Chang, "Detection of subpixel spectral signatures in hyperspectral image sequences," in *Proc. American Society of Photogrammetry & Remote Sensing Annu. Meeting*, Reno, 1994, pp. 236–247.

[24] R. S. Resmini, M. E. Kappus, W. S. Aldrich, J. C. Harsanyi, and M. Anderson, "Mineral mapping with HYperspectral Digital Imagery Collection Experiment (HYDICE) sensor data at Cuprite, Nevada, U.S.A.," *Int. J. Remote Sensing*, vol. 18, no. 17, pp. 1553–1570, 1997.

[25] W. Farrand and J. C. Harsanyi, "Mapping the distribution of mine tailing in the Coeur d'Alene river valley, Idaho, through the use of constrained energy minimization technique," *Remote Sensing of Environment*, vol. 59, pp. 64–76, 1997.

[26] S. Haykin, *Adaptive Filter Theory*, 3rd ed. Englewood Cliffs, NJ: Prentice-Hall, 1996.

[27] O. L. Frost, III, "An algorithm for linearly constrained adaptive array processing," *Proc. IEEE*, vol. 60, pp. 926–935, 1972.

[28] B. D. Van Veen and K. M. Buckley, "Beamforming: A versatile approach to spatial filtering," *IEEE Acoust, Speech, Signal Processing Mag.*, pp. 4–24, Apr. 1988.

[29] R. Schalkoff, *Pattern Recognition: Statistical, Structural and Neural Approaches*. New York: Wiley, 1992.

[30] R. O. Duda and P. E. Hart, *Pattern Classification and Scene Analysis*. New York: Wiley, 1973.

[31] C.-I. Chang and H. Ren, "An experiment-based quantitative and comparative analysis of hyperspectral target detection and image classification algorithms," *IEEE Trans. Geosci. Remote Sensing*, vol. 38, pp. 1044–1063, Mar. 2000.

[32] C.-I. Chang, H. Ren, Q. Du, S.-S. Chiang, and A. Ifarraguerri, "An ROC analysis for subpixel detection," presented at the IEEE 2001 International Geoscience and Remote Sensing Symp., Sydney, Australia, July 24–28, 2001.

[33] C. E. Metz, "ROC methodology in radiological imaging," *Investigat. Radiol.*, vol. 21, pp. 720–723, 1986.

[34] H. Suzuki and J. Toriwaki, "Automatic segmentation of head MRI images by knowledge guided thresholding," *Computerized Med. Imag., Graphics*, vol. 15, no. 4, pp. 233–240, July–Aug. 1991.

[35] A. A. Green, M. Berman, P. Switzer, and M. D. Craig, "A transformation for ordering multispectral data in terms of image quality with implications for noise removal," *IEEE Trans. Geosci. Remote Sensing*, vol. 26, pp. 65–74, Jan. 1988.

[36] J. B. Lee, A. S. Woodyatt, and M. Berman, "Enhancement of high spectral resolution remote sensing data by a noise-adjusted principal components transform," *IEEE Trans. Geosci. Remote Sensing*, vol. 28, pp. 295–304, May 1990.

[37] C.-I. Chang and D. Heinz, "Subpixel spectral detection for remotely sensed images," *IEEE Trans. Geoscience Remote Sensing*, vol. 38, pp. 1144–1159, May 2000.

[38] C.-I. Chang, *Hyperspectral Imaging: Techniques for Spectral Detection and Classification*. New York: Kluwer Academic, 2003.

[39] C.-I. Chang, "Target signature-constrained mixed pixel classification for hyperspectral imagery," *IEEE Trans. Geosci. Remote Sensing*, vol. 40, pp. 1065–1081, May 2002.

[40] C.-I. Chang, H. Ren, and S. S. Chiang, "Real-time processing algorithms for target detection and classification in hyperspectral imagery," *IEEE Trans. Geosci. Remote Sensing*, vol. 39, pp. 760–768, Apr. 2001.